RESEARCH ARTICLE

Journal of Optics and Photonics Research 2025, Vol. 2(4) 245–253

DOI: 10.47852/bonviewJOPR52024293



Lithium Niobate-Based MMI-MZI Electro-optic Switches with Lower Phase Shift Voltage

Md Koushik Alam^{1,*} , Noor Afsary¹, Md Nasir Uddin¹, A. K. M. Naim Ishtiaq¹ and Md Omar Faruk Rasel¹

¹Physics Discipline, Khulna University, Bangladesh

Abstract: Optical switches that effectively isolate outputs are crucial for precisely and efficiently directing and controlling optical signals. This study presents the design and characterization of a 1×2 electro-optic (EO) switch utilizing few-mode waveguides on a lithium niobate on insulator (LNOI) platform. Simulations conducted with the beam propagation method revealed equal splitting between outputs at 0 volts. When 1 volt was applied, the output switched to the bar port of the multimode interferometers (MMI), and at 3.5 volts, the output switched to the cross port of the MMI at a wavelength of $1.55 \, \mu m$. The device, measuring $6.56 \, mm$ in length, exhibits a voltage efficiency of $1.66 \, V \cdot cm$. The switch shows minimal insertion loss of $1.85 \, dB$ for output 1 and $1.87 \, dB$ for output 2, ensuring efficient signal transmission. Additionally, it maintains low crosstalk levels of $-30 \, dB$ and $-27.72 \, dB$ for output 1 and output 2, respectively, indicating effective isolation between output channels.

Keywords: phase shift voltage, electro-optic switch, multimode interference, Mach-Zehnder interferometer, lithium niobate

1. Introduction

Optical switches are essential components in modern communication networks and optical systems, enabling rapid and precise control over the transmission of optical signals. To meet the increasing demands of telecommunications and data communication systems, various optical switches have been developed, focusing on compact size, low-power consumption, and high-speed switching [1-6]. These switches are generally classified into electro-optic (EO) and thermo-optic (TO) switches based on their operating principles. TO switches function by leveraging the temperature dependence of the refractive index in optical waveguides. Known for their robustness and stability, these switches utilize guided light waves and feature simple circuitry, making them suitable for smallto-medium-scale optical switching applications. However, their switching speeds range from 100 microseconds to several milliseconds [7]. In contrast, EO switches exploit the EO effect, where the refractive index of a material changes in response to an applied electric field, to redirect or modulate light signals within optical fibers or integrated photonic circuits [8]. EO switches offer several advantages, including high-speed operation, low insertion loss (IL), compact size, and compatibility with existing optical infrastructure [8-10]. Their versatility and efficiency make them indispensable in telecommunications, data centers, sensing systems, and other applications.

Lithium niobate (LiNbO₃) is a highly advantageous material for EO switching technology due to several compelling reasons. Its exceptional EO properties [10–13] enable efficient modulation of light signals through the application of an external electric field. This characteristic is ideal for developing EO devices, such as modulators and switches [14–16], where fast and precise control of

optical signals is essential. Additionally, LiNbO₃ boasts a high nonlinear optical coefficient [13, 17, 18], facilitating the generation of nonlinear optical effects [19] such as frequency doubling and parametric amplification, critical for advanced photonic applications [19–21]. Its wide transparency range, extending from ultraviolet to mid-infrared [11], enhances its versatility for various applications. Furthermore, LiNbO₃ is noted for its excellent optical damage resistance, thermal stability, and compatibility with integrated optic technologies [16, 22], making it a preferred material for advancing optical communication systems and integrated photonic circuits.

Compared to other EO switches, those based on Mach-Zehnder interferometers (MZI) and multimode interferometers (MMI) receive significantly more attention. This is due to their exceptional performance features, including low IL, high extinction ratio, and fast switching speeds. Their unique design leverages interference effects and multimode properties, making them versatile for various telecommunications and data center applications. Researchers have explored multiple configurations of EO switches in MMI and MZIassisted MMI structures [15, 20, 23-27]. Chen et al. [20] introduced an EO switch employing an MMI-MZI configuration with thin-film LiNbO₃, showing a switching voltage of approximately 7.3 V and an extinction ratio of about 16 dB. However, this setup still exhibits high energy requirements and performance limitations concerning polarization states. Yu et al. [24] reported an EO polymer MMI waveguide switch with tapered access waveguides, showcasing promising features such as controlled changes in refractive index, a significant switching effect, and low crosstalk. However, this device requires an extended length of 5355 \times 40 μ m². Li et al. [26] presented a polymer-based EO switch in an MZI-assisted MMI configuration, which required a driving voltage of ±10 V and a highly sensitive MMI width. Masuda et al. [27] reported an EO switch within an MMI-MZI structure using lead zirconate titanate films, demonstrating a reduced switching voltage of 4.8V and an IL of 2-3 dB. While this indicates lower energy consumption than

^{*}Corresponding author: Md Koushik Alam, Physics Discipline, Khulna University, Bangladesh. Email: ms231732@ku.ac.bd

[©] The Author(s) 2025. Published by BON VIEW PUBLISHING PTE. LTD. This is an open access article under the CC BY License (https://creativecommons.org/licenses/by/4.0/).

previous reports, further optimization is needed to achieve lower operating voltages, compact footprint, and higher extinction ratios for enhanced device performance.

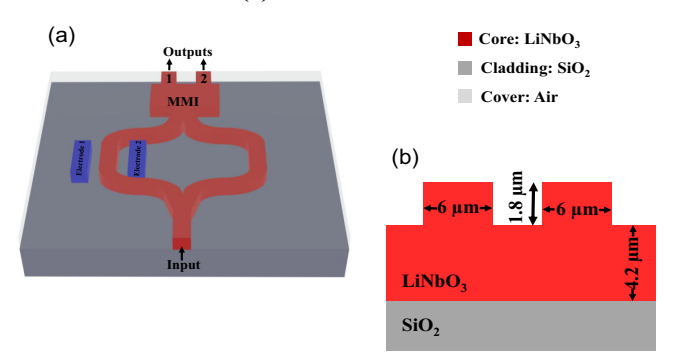
In this paper, we present a 1×2 EO switch integrated into a lithium niobate on insulator (LNOI) platform using few-mode waveguides within an MZI-assisted MMI splitter. Utilizing fewmode waveguides addresses key limitations in previous EO switch designs by providing a compact, efficient, and low-power solution. The proposed switch features a compact MMI structure measuring $419 \times 22 \mu m^2$, facilitating integration into densely packed photonic circuits and meeting the need for scalable and practical optical components in advanced communication systems. Our EO switch demonstrates equal splitting between outputs at 0 volts; when 1 volt is applied, the output switches to the bar port of the MMI, and at 3.5 volts, the output switches to the cross port, showcasing lower switching voltages than earlier models. The switch exhibits minimal crosstalk of -30 dB, indicating effective isolation between input and output channels. This achievement highlights the potential of the proposed design in overcoming the limitations commonly encountered in EO switch implementations, thereby enhancing the performance and scalability of optical communication systems.

2. Design and Optimization

2.1. Structural design

The operation of the EO switch relies on the modulation of a material's refractive index via an external electric field, thereby controlling the transmission of light signals. This functionality is pivotal for enhancing the reliability and flexibility of optical communication networks. In our study, we introduce and design a 1 × 2 EO switch utilizing a MZI-assisted MMI configuration, illustrated in Figure 1(a). The switch incorporates a ridge waveguide structure comprising LiNbO3 as the core material, silicon dioxide as the cladding, and air as the cover material. Our device features two electrodes, employed to apply an external electric field to the arms of the MZI. This modulation of the refractive index enables precise control of light transmission into output 1 and output 2, thereby facilitating the switching functionality. MMI devices exploit selfimaging within a multimode waveguide, where an input field profile is replicated in single or multiple images at regular intervals along the guide's propagation direction. For an in-depth examination of the self-imaging principle, particularly focusing on full-modal propagation analysis, readers are referred to [28]. Within the context

Figure 1
Overview of the EO switch: (a) 3D representation and (b) cross-sectional view



of a multimode waveguide, the beat length of the two lowest-order modes is expressed by Equation (1) as follows:

$$L_r = \frac{\pi}{\beta_0 - \beta_i} = \frac{4W_{eff}^2 n_f}{3\lambda} \tag{1}$$

where β_0 and β_i are the propagation constants of the fundamental and first-order modes, respectively, n_f is the ridge effective index, λ is the free-space wavelength, and W_{eff} is the effective waveguide width given by Eq. (2) demonstrated in [28]:

$$W_{eff} = W + \left(\frac{\lambda}{\pi}\right) \left(\frac{n_x}{n_f}\right)^{2z} \left(n_f^2 - n_x^2\right)^{-1/2}$$
 (2)

where n_x and W are the surrounding effective index and MMI waveguide width, respectively. For our proposed device, the beat length, L_r is calculated to be 418.72 μ m, and the effective width, W_{eff} is calculated to be 22.05 μ m.

The output field distribution emerging from the MMI waveguide is given by Equations (3a) and (3b) following matrix equation [26]:

$$E_{output}(1) = \frac{1}{\sqrt{2}} \left(E_{input} + E_{input} e^{\frac{i\tau}{2}} \right)$$
 (3a)

$$E_{output}(2) = \frac{1}{\sqrt{2}} \left(E_{input} e^{\frac{i\pi}{2}} + E_{input} \right)$$
 (3b)

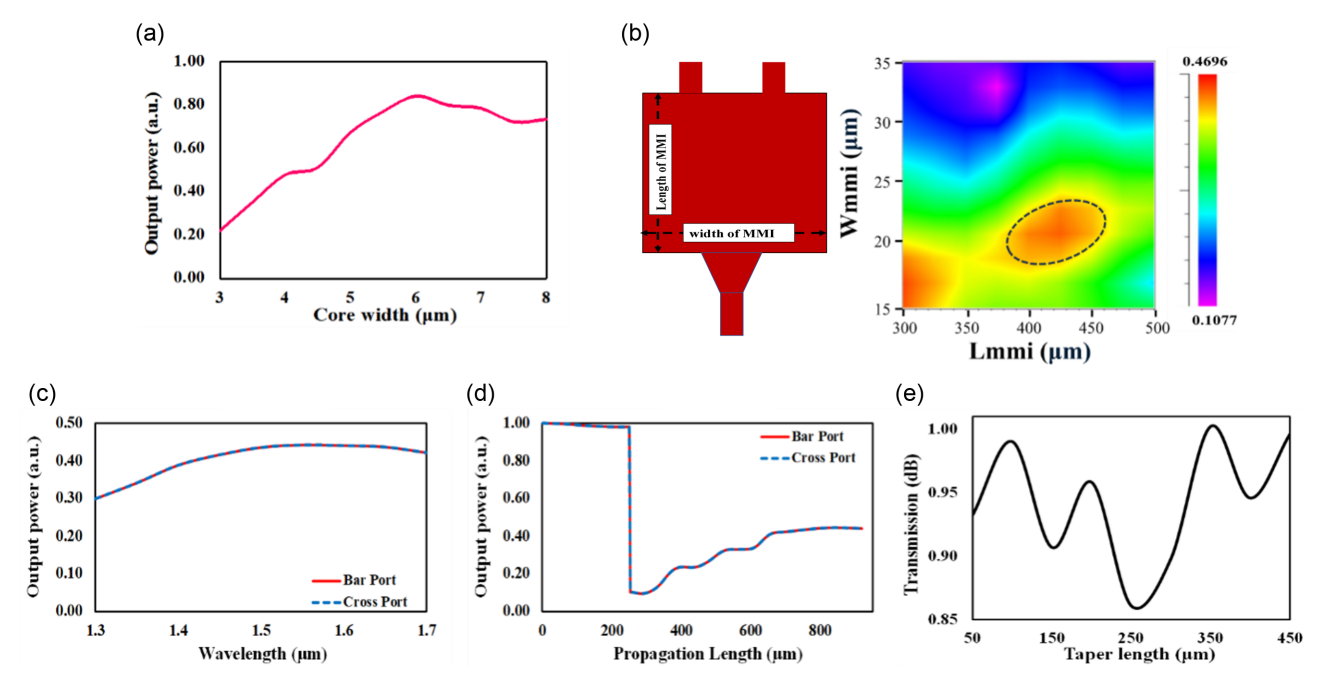
where E_{input} is the optical fields at the input port and E_{output} (1) and E_{output} (2) are the optical fields at the output ports 1 and 2. A cross-sectional view of the device is depicted in Figure 1(b), with the core width set at 6 μ m and a slab height of 4.2 μ m.

The proposed fabrication process of the EO switch involves multiple steps of lithography and material deposition, as illustrated in [21, 29, 30]. Initially, a thin layer of SiO₂ is deposited onto the substrate through chemical vapor deposition (CVD) to serve as the cladding material. Subsequently, a layer of LiNbO3 is deposited on top of the SiO₂ to form the core of the waveguide structure. Lithography techniques are then used to define the ridge structure. The LiNbO₃-coated substrate is coated with a photoresist layer, which is exposed to UV light through a mask that defines the desired ridge pattern. Following exposure, the unexposed regions of the photoresist are removed, leaving behind the patterned resist layer. Next, a dry or wet etching process selectively removes the LiNbO₃ layer in areas not shielded by the patterned resist, thereby forming the ridge structure. This etching exposes the underlying SiO₂ substrate in non-ridge areas. Finally, any residual photoresist is stripped away, leaving the fabricated ridge waveguide structure with LiNbO₃ as the core and SiO₂ as the cladding.

2.2. Structural parameter optimization

Optimizing the core width of an optical waveguide improves performance and reduces transmission errors by minimizing modal dispersion and enhancing signal integrity [16, 31]. As shown in Figure 2(a), we varied the core width of this device from 3 μ m to 8 μ m, finding that a 6 μ m core width yields the highest output efficiency compared to others. Thus, we choose 6 μ m as optimum core width. In the optimization process of the MMI device within an MZI-assisted MMI EO switch, careful consideration of its length and width is paramount, as they profoundly influence performance by regulating light transmission between device outputs [32]. Through meticulous adjustment of the Length (L_{MMI}) and Width (W_{MMI}) parameters of the MMI, we

 $Figure~2\\ Parameter optimization.~(a)~Core~width.~(b)~L_{MMI}~along~with~W_{MMI}.~(c)~light~propagation~into~the~MMI~(d)~Uniform~light~propagation~at~1.55~\mu m.~(e)~Taper~length~in~terms~of~transmission$



can precisely tailor its optical characteristics. Visual aids in Figure 2(b) offer schematic representations to aid in understanding the geometric dimensions under scrutiny. The color-coded illustration depicts the intensity distribution, with the red region signifying the highest intensity and the black-marked area indicating a high-intensity zone. To systematically explore and optimize the MMI device, we conducted investigations by varying L_{MMI} within the range of 300 μm to 500 μm , while simultaneously adjusting W_{MMI} between 15 μm to 35 μm. This endeavor aimed to pinpoint the optimal values for L_{MMI} and W_{MMI} that would yield the most uniform intensity distribution across the MMI output. Following exhaustive exploration, the tolerance range was determined to be 382 μm to 465 μm for L_{MMI} and 18 μm to 24 μm for $W_{MMI},$ within which the MMI exhibited maximum intensity uniformity. We also calculate the individual output power at the two ports of the MMI, namely the Bar port and the Cross port. Our goal is to achieve maximum uniformity between these two output ports, as illustrated in Figure 2(c). By varying the wavelength from 1.3 μm to 1.7 μm, we observe that the maximum output intensity occurs at 1.55 µm, which aligns with the device's primary optimization at this wavelength. Additionally, we illustrate the light propagation within the MMI at 1.55 µm in terms of the power distribution across the two output ports. The graph shows that both the bar port and cross port exhibit maximum output uniformity, resulting overlapping lines.

Upon completing the thorough optimization of the MMI, attention turned towards identifying the optimum taper length, a critical parameter influencing the performance of optical waveguides. The role of tapper waveguide is pivotal in ensuring the efficient insertion of the maximum amount of light into the waveguide. In this study, the taper length was systematically varied from 50 μm to 450 μm , as depicted in Figure 2(e). Graphical representation reveals that the lowest transmission loss occurs at a taper length of 250 μm . Consequently, we selected this value as

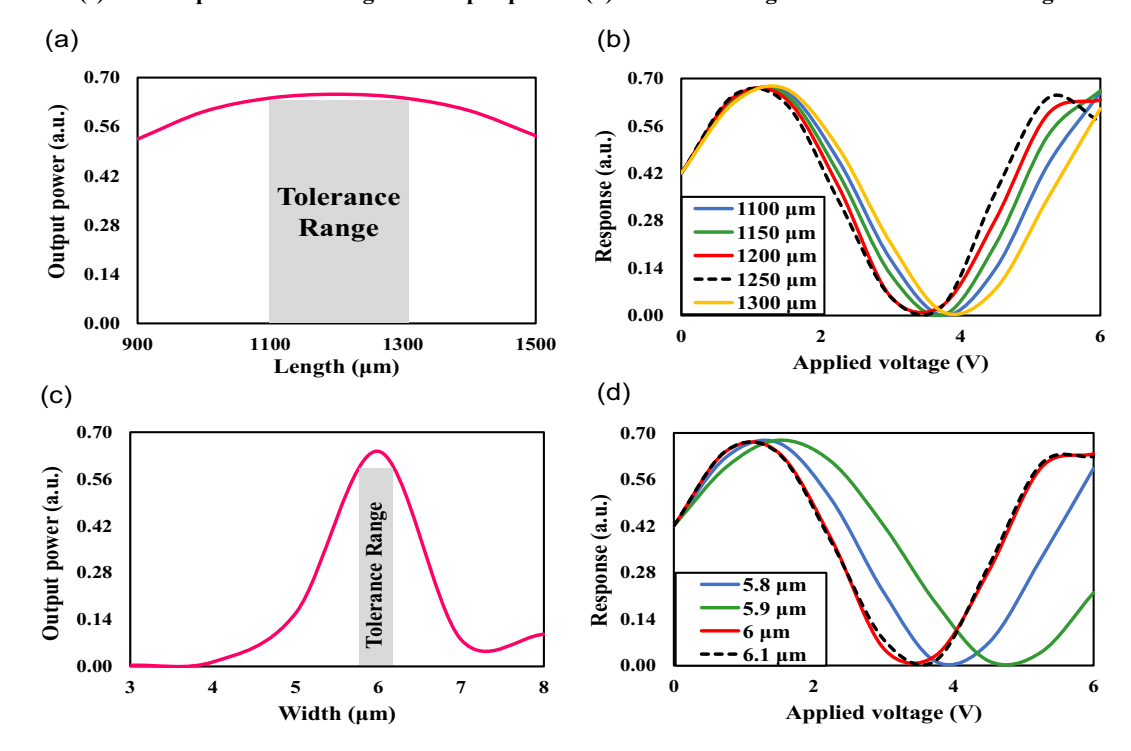
optimized for our EO switch. We selected the range of L_{MMI} starting from 300 μm , as this length is necessary to produce the first fold of multimode interference. The W_{MMI} was set at 15 μm ; below this value, the outputs tend to overlap, merging into a single output. This width helps maintain a proper gap between outputs and reduces crosstalk during optical switching. For the taper length, we started at 50 μm to minimize coupling losses associated with abrupt changes in core diameter, ensuring a more gradual transition. Our main goal is to use this arbitrary range for length and width optimization to achieve the most efficient output in the most compact component size.

It is imperative to optimize the height and width of the electrode to facilitate efficient switching through the EO effect. We optimized the electrode as depicted in Figure 3. Initially, we focused on optimizing the height of the electrode concerning the disparity between the ON and OFF states' output power, as illustrated in Figure 3(a). Differences in output powers indicate optimum switching. We varied the height from 900 μm to 1500 μm to determine the optimum height. The figure shows that the optimal tolerance range falls within 1100 μm to 1300 μm , where the maximum output power is achieved. Figure 3(b) displays the variation of the applied voltage corresponding to the height obtained from the tolerance range. The figure demonstrates that a height of 1200 μm exhibits the lowest first-phase shift voltage at 1 V and second-phase shift voltage at 3.5 V, with the voltage range varying from 1 V to 1.6 V and 3.5 V to 3.9 V, respectively.

After determining the electrode's optimum length, we optimized the electrode's width relative to the output power (the difference between the output power of the ON and OFF states), as depicted in Figure 3(c). The electrode width varied from 3 μ m to 8 μ m, and the tolerance range was identified between 5.8 μ m to 6.1 μ m. Similarly, we evaluated the effect of voltage on our proposed device with this width variation, as shown in Figure 3(d). This figure illustrates that an electrode width of 6 μ m

Figure 3

Electrode optimization. (a) Height optimization for output power. (b) Effect of the voltage within the tolerance range. (c) Width optimization along with output power. (d) Effect of voltage within the tolerance range



exhibits the lowest applied voltage to induce first- and second-order phase shift, with the voltage range varying from 1 V to $1.8~\mathrm{V}$ and $3.5~\mathrm{V}$ to $4.8~\mathrm{V}$.

3. Results and Discussion

3.1. EO switching

An EO switch is a critical element in optical communication systems, offering precise control over the phase modulation of optical signals [33]. This study highlights the sophisticated integration of electrodes into a MZI structure, as depicted in Figure 1. In our investigation, we vary the voltage of electrode 1 while electrode 2 is kept grounded. Since electrode 1 is symmetric to electrode 2 in terms of material, dimension, and separation gap from the arms of the MZI, the same results are obtained if electrode 1 is kept grounded and voltage is applied to electrode 2. We varied the voltage range from 0 V to 6 V to determine the phase shift voltage of our proposed switch, as depicted in Figure 4(a). The graph shows that at 1 V, the switch starts phase shifting, resulting in output 1 being in the ON state while output 2 is in the OFF state. At 3.5 V, output 1 transitions to the OFF state while output 2 transitions to the ON state. The separation gap between the electrode and the voltage interaction arm is crucial in achieving practical EO switching. We analyzed the tolerance range of this gap for the MZI. By varying the electrode gap from 0 μm to 4 μm, we determined the optimal electrode gap, as shown in Figure 4(b). The figure illustrates that the tolerance range lies between 1 µm and 2.5 µm. We calculate the phase shift voltage by varying the electrode gap within this tolerance range to identify the most optimized voltage effect, as demonstrated in Figure 4(c). The first-phase shift voltage varies within the range of 1 V to 1.3 V and second-phase shift voltage varies from 3.5 V to 3.75 V. Notably, the electrode gaps of 1.5 μ m and 2 μ m exhibited the most minimal voltage for both phase shift for this EO switch. In our simulation process, we defined the electrodes and specified the EO parameters of the materials as follows: r13 = 9.6 pm/V, r22 = 6.8 pm/V, and r33 = 30.9 pm/V, d31 = -4.8382 pm/V, d33 = -25 pm/V [34].

Reducing phase shift voltage depends upon interaction length between the light and the electric field and reducing the electrode gap between the electrodes and waveguides which results electric field overlap with the optical mode [16, 20]. The phase shift $\Delta \emptyset$ induced in an optical signal passing through an electro-optic material can be described by the equation:

$$\Delta \emptyset = \frac{2\pi}{\lambda} \Delta n L \tag{4}$$

Where λ is the wavelength, Δn is the change in the refractive index due to the applied electric field, L is the effective length of the optical path through which the light travels in the EO material. The change in refractive index Δn is related to the applied electric field E through the Pockels effect, which can be expressed as:

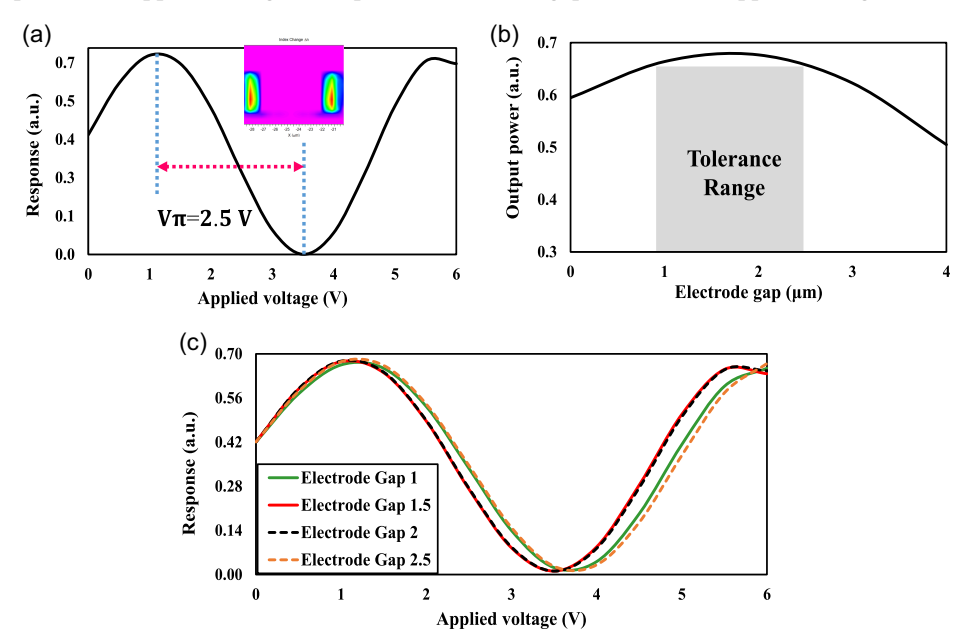
$$\Delta n = r.E \tag{5}$$

where r is the electro-optic coefficient of the material, typically expressed in units of pm/V. The electric field E in the region between the electrodes is given by the relationship:

$$E = \frac{V}{d} \tag{6}$$

Where V is the applied voltage and d represent the distance between the electrodes. By substituting E into the expression for Δn , it can be written as:

Figure 4
(a) Change of response with applied voltage. (b) Optimized electrode gap. (c) Effect of applied voltage in various electrode gap



$$\Delta n = r. \frac{V}{d} \tag{7}$$

Substituting this expression for Δn back into the phase shift equation gives:

$$\Delta \emptyset = \frac{2\pi}{\lambda} r \cdot \frac{V}{d} \cdot L \tag{8}$$

Rearranging this equation allows us to express the required voltage V for a given phase shift $\Delta \phi$ as follows:

$$V = \frac{\Delta\phi \,\lambda \,d}{2\pi rL} \tag{9}$$

The dimensions of the electrodes play a pivotal role in determining the effective electric field E, which is given by $E = \frac{V}{d}$. When the electrode height and width are optimized, the distance d between the electrodes is effectively reduced, allowing for a stronger electric field for a given applied voltage. This enhancement in electric field strength leads to a more substantial change in refractive index, thereby reducing the voltage required to achieve the desired phase shift.

Table 1 provides encapsulates the parameters governing the phase-shifting properties within this EO switch. $V\pi_1$ and $V\pi_2$ represent the applied voltage for inducing phase shifts between output 1 and output 2, respectively. This comprehensive approach showcases the intricacies of EO switches and underscores their potential significance in advancing optical communication technologies.

The parameters calculated above were applied to investigate the switching operation of our proposed EO switch, as depicted in

Table 1
The parameters for the phase-shifting voltage

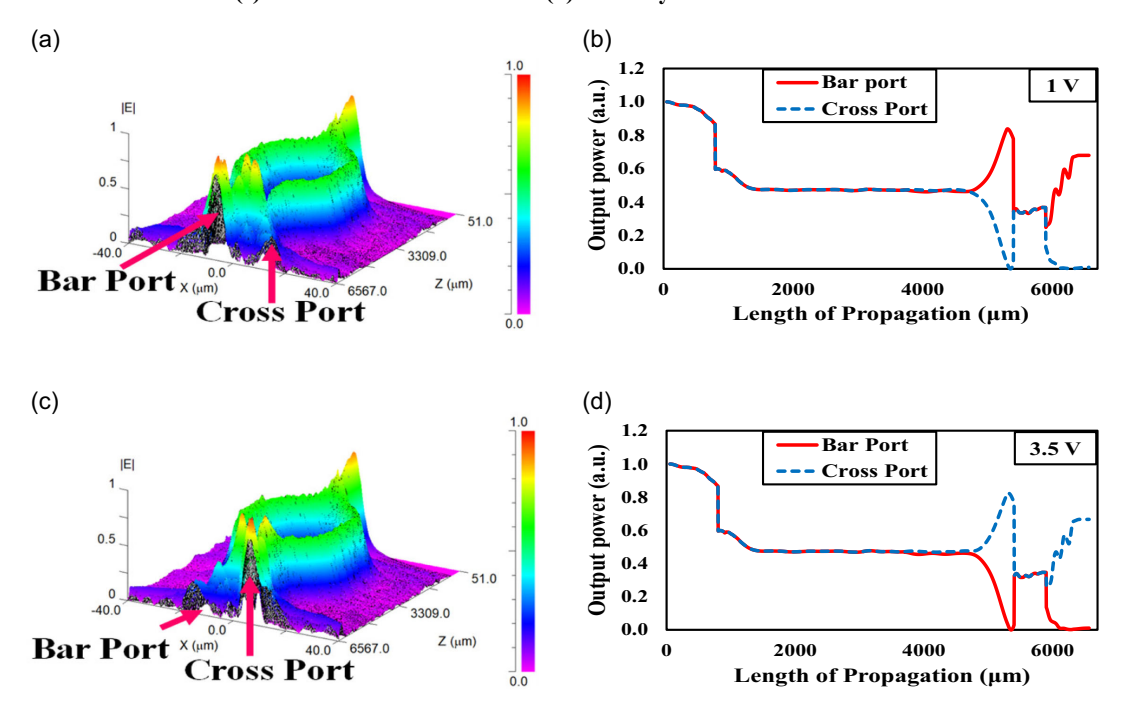
Voltage, Vπ (Volt)	Outputs				
1	Output 1 ON	Output 2 OFF			
3.5	Output 1 OFF	Output 2 ON			

Figure 5. Initially, a voltage of 1 V was applied, producing the simulation shown in Figure 5(a), where the x coordinate represents the transverse direction (the horizontal position across the width of the waveguide or MMI structure), while the z coordinate represents the longitudinal or propagation direction along the length of the waveguide or MMI structure. This figure illustrates that output 1 (O₁) is in the ON state, while output 2 (O₂) is in the OFF state. The intensity distribution along the output power is displayed in Figure 5(b), with the red line representing output 1 and the blue line representing output 2. The result confirms that output 1 is ON, while output 2 is OFF. Subsequently, a voltage of 3.5 V was applied, leading to the simulation result shown in Figure 5(c). In this case, output 2 is in the ON state, while output 1 is in the OFF state. The corresponding intensity distribution and output power for this voltage are depicted in Figure 5(d), indicating that output 2 is ON, while output 1 remains OFF.

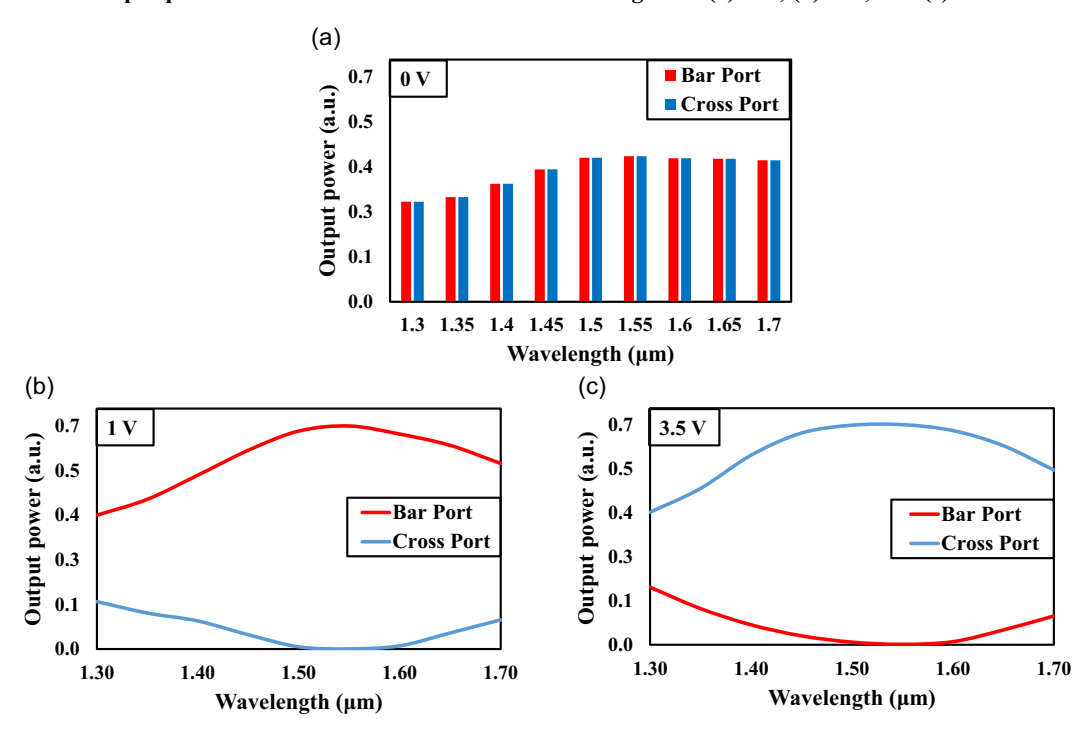
This device has been optimized for operation at a wavelength of 1.55 μ m. Consequently, we investigate the performance of the switch across a wavelength range from 1.3 μ m to 1.7 μ m, as depicted in Figure 6. In Figure 6(a), the output power of the optical switch is varied within the wavelength range of 1.3 μ m to 1.7 μ m at 0 V. The figure illustrates a gradual increase in output power up to 1.5 μ m, after which it remains relatively stable within the range of 1.5 μ m to 1.7 μ m. Similarly, in Figure 6(b), we analyze the output power variation at 1 V. The graph demonstrates that for the ON state, the output power gradually increases until reaching 1.55 μ m, which begins to decrease. The output power varies within the range of 0.4 a.u. to 0.68 a.u. For the OFF state, the output power gradually decreases until 1.55 μ m, then starts to increase again. The output power varies within the range of 0.1 a.u. to 0.0006 a.u.

Furthermore, we examine the output power variation at 3.5 V demonstrated in Figure 6(c). In this scenario, for the ON state, the output power increases until 1.55 μm and then decreases again, with a variation range of 0.4 to 0.67 a.u. For the OFF state, the output power decreases with increasing wavelength until 1.55 μm , then rises again, with a variation range of 0.12 a.u. to 0.001 a.u. These investigations provide valuable insights into the behavior of

Figure 5
Switching operation. (a) Simulation result at 1 V. (b) Intensity distribution at 1 V. (c) Simulation result at 3.5 V. (d) Intensity distribution at 3.5 V



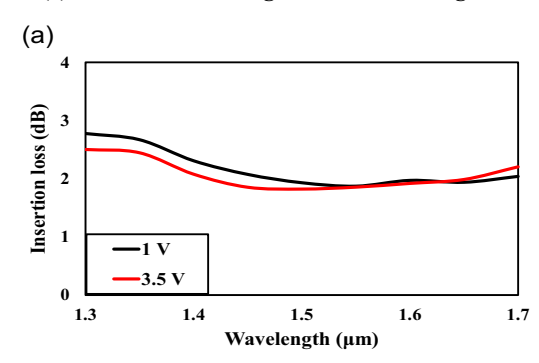
 $Figure\ 6$ Output power variation in terms of different wavelengths at (a) 0 V, (b) 1 V, and (c) 3.5 V



the switch across different wavelengths and voltage settings, facilitating a comprehensive understanding of its performance characteristics in practical applications for real-world applications, particularly in high-speed optical communications and integrated photonic circuits [18, 35]. Lowering the phase shift voltage minimizes power consumption, which is essential

for energy-efficient operation in dense photonic systems [12, 14, 36]. Additionally, the ability to achieve significant phase shifts with such low voltages allows for more compact designs, where integration of multiple optical functionalities becomes feasible without excessive power draw or thermal management challenges.

Figure 7
(a) Insertion loss along with the wavelength variation and (b) insertion loss along the applied voltage



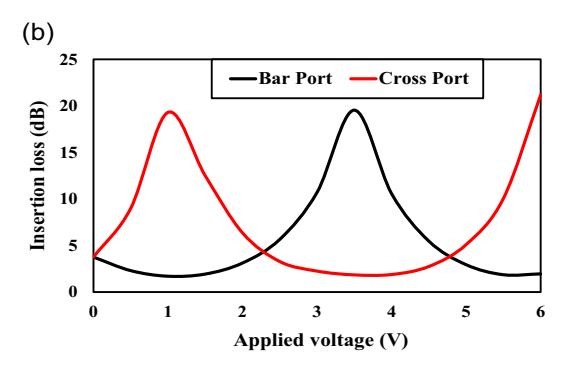


Figure 7(a), the IL is depicted alongside the wavelength variation.

Notably, when a voltage of 1 V is applied, the excess loss

gradually decreases until reaching 1.55 µm, where it almost

stabilizes across the remaining region. However, upon application of 3.5 V, the excess loss follows a decreasing trend until 1.5 µm,

beyond which it starts increasing again. At the critical wavelength

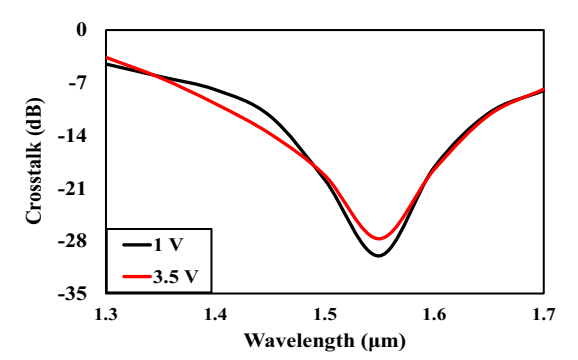
of 1.55 μm , the IL measures 1.85 dB for 1 V and 1.87 dB for 3.5 V.

corresponds to Output 2. The graph illustrates that the IL ranges from 1.85 dB to 19.15 dB for output 1, showing a lower IL at 1 V

when output 1 is ON. In this scenario, the IL of output 2 is 21.18

In Figure 7(b), we observe the variation of IL concerning applied voltage. The black line represents Output 1, while the red line

Figure 8
Crosstalk for the wavelength



dB as it is in the OFF. Conversely, the IL ranges from 1.87 dB to 21.18 dB, with a lower IL observed at 3.5 V when output 2 is in the ON, while output 1 exhibits a 19.15 dB IL when it is in the OFF.

3.2. Loss calculation

3.2.1. IL analysis

IL is crucial for EO switches as it quantifies the amount of signal attenuation during switching [37], aiding in assessing signal integrity and overall switch performance in optical communication systems. We carefully calculate the excess loss by using the following equation [38]:

$$IL = -10 \log 10 \left(\frac{\sum_{i=1}^{n} P_{\text{out}}}{P_{\text{in}}} \right)$$
 (10)

In this set of equations, P_{out} denotes the output power, while P_{in} stands for the input power of the switch. The research investigates the optical switch's performance across a range of wavelengths spanning from 1.3 μ m to 1.7 μ m, as illustrated in Figure 7. In

3.2.2. Crosstalk analysis

Crosstalk refers to unwanted interference or signal leakage between channels in a communication system [39]. In an EO switch, measuring crosstalk is crucial as it indicates the extent to which switching operations affect adjacent channels, ensuring signal integrity and minimizing errors in data transmission. In this study, we determine the crosstalk by analyzing different wavelengths with the equation demonstrated in [40]:

$$Crosstalk = 10log_{10} \left(\frac{P_{Unwanted}}{P_{Desired}} \right)$$
 (11)

where $P_{Unwanted}$ and $P_{Desired}$ indicate the unwanted and desired optical power of the outputs. The variation of crosstalk is depicted in Figure 8. The black line indicates the crosstalk of output 1, and the red line indicates the crosstalk of output 2.

Table 2
Comparison of this work with existing EO switch

	Half wave	Insertion					
Configuration	voltage (V)	loss (dB)	Crosstalk (dB)	Footprint (mm ²)	Material	Method	References
MMI	1	_	-30	4.3×0.04	Polymer	Simulation	[24]
MMI-DC	4.1	0.64	-13.66	4.09×0.05	LNOI	Simulation	[15]
MMI-MZI	±10	1.8	-25	11.96×0.04	Polymer	Simulation	[26]
MMI-MZI	7.3	~13	~-16	_	LNOI	Experimental	[20]
MMI-MZI	4.8	2-3	_	6.50×0.03	PLZT	Experimental	[27]
MMI-MZI	2.5	1.85	-30	6.57×0.04	LNOI	Simulation	This work

Note: *LNOI = Lithium Niobate on Insulator, PLZT = Lanthanum-modified Lead Zirconate Titanate

We varied the wavelength of the EO switch from 1.3 μm to 1.7 μm and calculated the crosstalk. Crosstalk gradually decreases as the wavelength increases until it reaches its lowest point at 1.55 μm , then rises again. Thus, the crosstalk ranges from -4.51 dB to -30 dB for output 1, and from -3.62 dB to -27.72 dB for output 2. The minimal crosstalk is obtained at -30 dB for output 1 and -27.72 dB for output 2 at 1.55 μm for this EO switch. Table 2 presents the performance comparison of different EO switches with this proposed EO switch.

4. Conclusion

In conclusion, we have introduced a novel 1×2 EO switch integrated within a MZI-assisted multimode interference (MMI) splitter on the LNOI platform. This switch enables precise control of optical signals through external voltage-induced phase shifts by leveraging a compact MMI structure. These switches exhibit a low phase shift voltage for the first-phase shift at 1 V, and a subsequent phase shift is at 3.5 V (specifically at a wavelength of 1.55 μ m). Notably, the switch demonstrates minimal IL (1.85 dB for output 1 and 1.87 dB for output 2) and effectively isolates input and output channels (crosstalk levels of -30 dB for output 1 and -27.72 dB for output 2). These promising results highlight the potential of our proposed switches to address the voltage and crosstalk limitations, thereby enhancing the performance and scalability of future high-speed communication systems.

Ethical Statement

This study does not contain any studies with human or animal subjects performed by any of the authors.

Conflicts of Interest

The authors declare that they have no conflicts of interest to this work.

Data Availability Statement

Data are available from the corresponding author upon reasonable request.

Author Contribution Statement

Md Koushik Alam: Conceptualization, Methodology, Formal analysis, Resources, Data curation, Writing — original draft, Visualization. Noor Afsary: Software, Formal analysis, Writing — original draft. Md Nasir Uddin: Formal analysis, Investigation, Writing — review & editing. A. K. M. Naim Ishtiaq: Formal analysis, Data curation, Writing — review & editing. Md Omar Faruk Rasel: Conceptualization, Writing — review & editing, Supervision.

References

- [1] Tu, X., Song, C., Huang, T., Chen, Z., & Fu, H. (2019). State of the art and perspectives on silicon photonic switches. *Micromachines*, 10(1), 51. https://doi.org/10.3390/mi10010051
- [2] Soref, R. (2018). Tutorial: Integrated-photonic switching structures. APL Photonics, 3(2), 021101. https://doi.org/10. 1063/1.5017968
- [3] Thomaschewski, M., Zenin, V. A., Wolff, C., & Bozhevolnyi, S. I. (2020). Plasmonic monolithic lithium niobate directional coupler switches. *Nature Communications*, 11(1), 748. https://doi.org/10.1038/s41467-020-14539-y

- [4] Gao, S., Xu, M., He, M., Chen, B., Zhang, X., Li, Z., ..., & Cai, X. (2019). Fast polarization-insensitive optical switch based on hybrid silicon and lithium niobate platform. *IEEE Photonics Technology Letters*, 31(22), 1838–1841. https://doi.org/10.1109/lpt.2019.2949090
- [5] Song, Q. Q., Chen, K. X., & Hu, Z. F. (2020). Low-power broadband thermo-optic switch with weak polarization dependence using a segmented graphene heater. *Journal of Lightwave Technology*, 38(6), 1358–1364. https://doi.org/10. 1109/jlt.2019.2955511
- [6] Kita, T., & Mendez-Astudillo, M. (2021). Ultrafast silicon MZI optical switch with periodic electrodes and integrated heat sink. *Journal of Lightwave Technology*, 39(15), 5054–5060. https://doi.org/10.1109/jlt.2021.3082634
- [7] Hauffe, R., & Petermann, K. (2006). Thermo-optic switching. In T. S. El-Bawab (Ed.), *Optical switching* (pp. 111–139). Springer. https://doi.org/10.1007/0-387-29159-8_4
- [8] Sinatkas, G., Christopoulos, T., Tsilipakos, O., & Kriezis, E. E. (2021). Electro-optic modulation in integrated photonics. *Journal of Applied Physics*, 130(1), 010901. https://doi.org/ 10.1063/5.0048712
- [9] Hou, S., Hu, H., Liu, Z., Xing, W., Zhang, J., & Hao, Y. (2024). High-speed electro-optic modulators based on thin-film lithium niobate. *Nanomaterials*, 14(10), 867. https://doi.org/10.3390/ nano14100867
- [10] Zhang, M., Wang, C., Kharel, P., Zhu, D., & Lončar, M. (2021). Integrated lithium niobate electro-optic modulators: When performance meets scalability. *Optica*, 8(5), 652–667. https:// doi.org/10.1364/optica.415762
- [11] Leidinger, M., Fieberg, S., Waasem, N., Kühnemann, F., Buse, K., & Breunig, I. (2015). Comparative study on three highly sensitive absorption measurement techniques characterizing lithium niobate over its entire transparent spectral range. *Optics Express*, 23(17), 21690–21705. https://doi.org/10.1364/OE.23.021690
- [12] Liu, J., Qu, L., Wu, W., Jin, C., Chen, Z., Gu, Z., ..., & Xu, J. (2024). Lithium niobate thin film electro-optic modulator. Nanophotonics, 13(8), 1503–1508. https://doi.org/10.1515/nanoph-2023-0865
- [13] Gorkunov, M., Sturman, B., Luennemann, M., & Buse, K. (2003). Feedback-controlled two-wave coupling in reflection geometry: Application to lithium niobate crystals subjected to extremely high external electric fields. *Applied Physics B*, 77(1), 43–48. https://doi.org/10.1007/s00340-003-1258-8
- [14] Li, M., Ling, J., He, Y., Javid, U. A., Xue, S., & Lin, Q. (2020). Lithium niobate photonic-crystal electro-optic modulator. *Nature Communications*, 11(1), 4123. https://doi.org/10.1038/s41467-020-17950-7
- [15] Afsary, N., Alam, M. K., Hoque, K., & Rasel, M. O. F. (2024). High-performance electro-optic switches with compact multimode interference and Bezier S-bend waveguides. *Journal of Physics: Photonics*, 6(3), 035014. https://doi.org/ 10.1088/2515-7647/ad4c40
- [16] Afsary, N., Alam, M. K., Rasel, M. O. F., & Ishigure, T. (2024). Thermally reliable compact electro-optic modulators with a low half-wave voltage. *Optics Continuum*, *3*(6), 1012–1024. https://doi.org/10.1364/optcon.524525
- [17] You, B., Yuan, S., Tian, Y., Zhang, H., Zhu, X., Mortensen, N. A., & Cheng, Y. (2024). Lithium niobate on insulatorfundamental opto-electronic properties and photonic device prospects. *Nanophotonics*, 13(17), 3037–3057. https://doi. org/10.1515/nanoph-2024-0132

- [18] Sun, X., Liang, H., Luo, R., Jiang, W. C., Zhang, X. C., & Lin, Q. (2017). Nonlinear optical oscillation dynamics in high-Q lithium niobate microresonators. *Optics Express*, 25(12), 13504–13516. https://doi.org/10.1364/oe.25.013504
- [19] Zheng, Y., & Chen, X. (2021). Nonlinear wave mixing in lithium niobate thin film. *Advances in Physics: X*, 6(1), 1889402. https://doi.org/10.1080/23746149.2021.1889402
- [20] Chen, Q., Wang, M. K., Ma, X. X., Yao, H., & Chen, K. X. (2022). Broadband and low-random-phase-errors 2 × 2 optical switch on thin-film lithium niobate. *IEEE Photonics Journal*, 14(6), 6664105. https://doi.org/10.1109/jphot.2022.3228264
- [21] Yang, S., Xu, J., Li, Y., Wu, L., Quan, X., Fu, L., ..., & Cheng, X. (2021). Highly-efficient thin film LiNbO₃ surface couplers connected by ridge-waveguide subwavelength gratings. *Journal of Materials Science: Materials in Electronics*, 32(17), 21932–21943. https://doi.org/10.1007/s10854-021-06599-7
- [22] Bazzan, M., & Sada, C. (2015). Optical waveguides in lithium niobate: Recent developments and applications. *Applied Physics Reviews*, *2*(4), 040603. https://doi.org/10.1063/1.4931601
- [23] Lu, G. W., Zhang, H. B., Shinada, S., Hong, J., Cheng, Y., & Yokoyama, S. (2021). Power-efficient O-band 40 Gbit/s PAM4 transmitter based on dual-drive cascaded carrier-depletion and carrier-injection silicon Mach-Zehnder modulator with binary driving electronics at CMOS voltages. *IEEE Journal of Selected Topics in Quantum Electronics*, 27(3), 3500308. https://doi.org/10.1109/jstqe.2021.3056721
- [24] Yu, F., Yamamoto, K., Piao, X., & Yokoyama, S. (2011). Multimode interference waveguide switch of electro-optic polymer with tapered access waveguides. *Physics Procedia*, 14, 25–28. https://doi.org/10.1016/j.phpro.2011.05.006
- [25] Thapliya, R., Nakamura, S., & Kikuchi, T. (2006). Electrooptic multimode interference device using organic materials. *Applied Optics*, 45(21), 5404–5413. https://doi.org/10.1364/ao.45.005404
- [26] Li, H. P., Liao, J. K., Tang, X. G., Lu, R. G., & Liu, Y. Z. (2009). 2 × 2 polymeric electro-optic MZI switch using multimode interference couplers. In 2009 International Conference on Optical Instruments and Technology: Optoelectronic Devices and Integration: Proceedings of SPIE, 7509, 75090X. https://doi. org/10.1117/12.837822
- [27] Masuda, S., Seki, A., Shiota, K., & Masuda, Y. (2011). Mach–Zehnder interferometer-type photonic switches based on epitaxially grown lanthanum-modified lead zirconate titanate films. *Journal of Lightwave Technology*, 29(2), 209–214. https://doi.org/10.1109/jlt.2010.2098394
- [28] Soldano, L. B., & Pennings, E. C. (1995). Optical multi-mode interference devices based on self-imaging: Principles and applications. *Journal of Lightwave Technology*, 13(4), 615–627. https://doi.org/10.1109/50.372474
- [29] Wang, C., Zhang, M., Chen, X., Bertrand, M., Shams-Ansari, A., Chandrasekhar, S., ..., & Lončar, M. (2018). Integrated lithium niobate electro-optic modulators operating at CMOS-compatible voltages. *Nature*, 562(7725), 101–104. https://doi.org/10.1038/ s41586-018-0551-y

- [30] Takigawa, R., & Asano, T. (2018). Thin-film lithium niobateon-insulator waveguides fabricated on silicon wafer by roomtemperature bonding method with silicon nanoadhesive layer. *Optics Express*, 26(19), 24413–24421. https://doi.org/10. 1364/oe.26.024413
- [31] Liu, H., She, X., Chen, M., Bi, R., Chen, K., Wang, L., & Shu, X. (2024). MMI waveguide reflector based on lithium niobate thin film. *Optics Communications*, *566*, 130706. https://doi.org/10.1016/j.optcom.2024.130706
- [32] Zhu, W., Deng, C., Wang, D., Wang, Q., Sun, Y., Wang, J., ..., & Cui, Y. (2024). Broadband and easily fabricated double-tip edge coupler based on thin-film lithium niobate platform. *Optics Communications*, *573*, 131031. https://doi.org/10.1016/j.optcom.2024.131031
- [33] Khalid, M., Ferraresi, S., Bellanca, G., Barbiroli, M., Fuschini, F., Tralli, V., ..., & Calò, G. (2024). LNOI wireless switches based on optical phased arrays for on-chip communication. *IEEE Journal on Selected Areas in Communications*, 42(8), 2054–2065. https://doi.org/10.1109/jsac.2024.3399207
- [34] Zhu, D., Shao, L., Yu, M., Cheng, R., Desiatov, B., Xin, C. J., ..., & Lončar, M. (2021). Integrated photonics on thin-film lithium niobate. *Advances in Optics and Photonics*, *13*(2), 242–352. https://doi.org/10.1364/aop.411024
- [35] Yin, Y., Xu, X., Lv, X., Tang, B., Zhang, P., & Zhang, D. (2023). 3 × 3 non-blocking SOI electro-optic switch. *IEEE Photonics Technology Letters*, 35(24), 1295–1298. https://doi.org/10.1109/lpt.2023.3311777
- [36] Gao, S., Xu, M., He, M., Chen, B., Zhang, X., Li, Z., ..., & Cai, X. (2019). Fast polarization-insensitive optical switch based on hybrid silicon and lithium niobate platform. *IEEE Photonics Technology Letters*, 31(22), 1838–1841. https://doi.org/10.1109/lpt.2019.2949090
- [37] Li, X., Lu, L., Zhou, Y., Bao, W., Chen, J., & Zhou, L. (2024). Low-loss and power-efficient polarization-diversity 4 × 4 microring switch on a multi-layer Si₃N₄-on-SOI platform. *Journal of Lightwave Technology, 43*(1), 230–238. https://doi.org/10.1109/jlt.2024.3449432
- [38] Alam, M. K., Afsary, N., Islam, M. Z., & Rasel, M. O. F. (2024). Investigation of polymer-based 1 × 2 all-optical switches at C-band wavelength. *Journal of Optics and Photonics Research*, *I*(2), 59–66. https://doi.org/10.47852/bonviewjopr42022168
- [39] Yin, Y., Xu, X., Lv, X., Tang, B., Zhang, P., & Zhang, D. (2023). 3 × 3 non-blocking SOI electro-optic switch. *IEEE Photonics Technology Letters*, 35(24), 1295–1298. https://doi.org/10.1109/lpt.2023.3311777
- [40] Alam, M. K., Afsary, N., Nijhum, Z. T., and Rasel, M. O. F. (2024). Polymer-based three-waveguide polarization beam splitter with reduced crosstalk for optical circuitry. *Applied Optics*, 63(12), 3265. https://doi.org/10.1364/ao.521414

How to Cite: Alam, M. K., Afsary, N., Uddin, M. N., Ishtiaq, A. K. M. N., & Rasel, M. O. F. (2025). Lithium Niobate-Based MMI-MZI Electro-optic Switches with Lower Phase Shift Voltage. *Journal of Optics and Photonics Research*, 2(4), 245–253. https://doi.org/10.47852/bonviewJOPR52024293